

---

# Flow Topology Beyond Skeletons: Visualization of Features in Recirculating Flow

Ronald Peikert and Filip Sadlo

Computer Graphics Laboratory, Computer Science Department,  
ETH Zurich, Switzerland, {peikert, sadlo}@inf.ethz.ch

**Summary.** A pattern often found in regions of recirculating flow is the vortex ring. Smoke rings and vortex breakdown bubbles are two familiar instances of this pattern. A vortex ring requires at least two critical points, and in fact this minimum number is observed in many synthetic or real-world examples. Based on this observation, we propose a visualization technique utilizing a Poincaré section that contains the pair of critical points. The Poincaré section by itself can be taken as a visualization of the vortex ring, especially if streamlines are seeded on the stable and unstable manifolds of the critical points. The resulting image reveals the extent of the structure, and more interestingly, regions of chaos and islands of stability. As a next step, we describe for the case of incompressible flow an algorithm for finding invariant tori in an island of stability. The basic idea is to find invariant closed curves in the Poincaré plane, which are then taken as seed curves for stream surfaces. For visualization the two extremes of the set of nested tori are computed. This is on the inner side the periodic orbit toward which the tori converge, and on the outer side, a torus which marks the boundary between ordered and chaotic flow, a distinction which is of importance for the mixing properties of the flow. For the purpose of testing, we developed a simple analytical model of a perturbed vortex ring based on Hill's spherical vortex. Finally, we applied the proposed visualization methods to this synthetic vector field and to two hydromechanical simulation results.

## 1 Introduction

Vector field topology, introduced by Helman and Hesselink [HH89], can be summarized as the use of concepts from the theory of continuous dynamical systems (see e.g. [GH83]) in scientific visualization. The main motivation for vector field topology is its ability to provide a condensed representation of a vector field. The most popular such representation is the topological skeleton which is usually defined as the set of all critical points and all separatrices. In two dimensions, the topological skeleton provides a segmentation of the domain into regions of similar flow behavior. The separatrices can be obtained by computing the stable and unstable manifolds of all critical points of saddle

type. However, unless the vector field is irrotational, there may also exist periodic orbits that behave like sources or sinks. If this is the case, the topological skeleton computed this way is incomplete. Only if the set of (isolated) periodic orbits is explicitly added to the skeleton, the full segmentation is obtained. An algorithm for finding isolated periodic orbits was developed by Wischgoll and Scheuermann [WS01].

When going to three dimensions, the topological skeleton can again be defined as the set of all critical points and all separatrices. The separatrices are the stable and unstable manifolds of saddles and spiral saddles (saddle foci), coming in pairs of a 1D and a 2D manifold, i.e. a streamline and a stream surface. The 1D manifolds are obviously not very useful for the purpose of segmenting a 3D domain. Only in the case of spiral saddles, they have some relevance, as they are sometimes understood as vortex core lines. The 2D manifolds theoretically provide segmentation, but in practical flows, these stream surfaces can become very convoluted. An alternative is to show only their pairwise intersections, known as saddle connectors [TWHS03] or heteroclinic orbits, resulting in a visualization of the connectivity between critical points.

The usage of vector field topology for scientific visualization is not restricted to showing topological skeletons. For example, critical points can be used for streamline placement [YKP05]. Even if the full set of critical points is used without any type analysis, this strategy was shown to yield effective visualizations by Weinkauff et al. [WHN\*03]. Alternatively, a visualization of the local flow behavior near critical points can be obtained by displaying icons showing the linearized flow defined by the critical point type and by the eigenvectors of the Jacobian of the vector field [GLL91]. The same information can be used to seed short streamlines near critical points [LDG98], giving a slightly more global picture of the flow.

It is interesting to notice that most work done so far in topology-based visualization falls in one of two categories, either giving a global picture of the entire domain or a local picture of neighborhoods of critical points. While global effects are an interesting part of dynamical systems and chaos theory, it can be argued that for flow visualization, they are less relevant because of issues such as domain boundaries, simulation accuracy, or time-dependence. But also the other extreme, independent visualization of critical points, can be regarded as unsatisfactory, since much of the topological information is left unused. We believe that vector field topology has much to offer for flow structures which fall in between the two extremes. One such structure is the vortex ring, which is essentially determined by two critical points and a small number of periodic orbits. In an earlier paper [SP07], we used a specialized stream surface algorithm for the visualization of such middle-scale flow features. Garth et al. [GTS\*04] and Tricoche et al. [TGK\*04] demonstrated how complex flow structures such as vortex breakdown bubbles can effectively be visualized by using stream surfaces and volume rendering, respectively. In

this paper we present complementary visualization techniques which are more closely oriented at the topology.

There has of course been previous work on visualization of dynamical systems. In particular for visualizing the behavior near critical points of a 3D system, Löffelmann et al. introduced various techniques such as glyphs [LDG98], Poincaré maps [LKG97] directly visualized in the context of the 3D field, and bundles of trajectories [LG98] rendered as illuminated streamlines [SZH97]. In all these cases, the object to be visualized was a given dynamical system. What we show in this work is that vector fields originating from other sources, such as synthetic flow fields or industrial CFD results, are just as well suited for being visualized as dynamical systems. In particular, we believe that is worth looking at further concepts of the dynamical systems theory than those which have made their way into the toolbox of vector field topology. As a source of inspiration, the book by Abraham and Shaw [AS92] can be recommended.

## 2 Topology of vortex rings

A typical feature occurring in recirculation regions is a connected pair  $(C_0, C_1)$  of critical points where  $C_0$  is a 1:2 spiral saddle (1 incoming and 2 outgoing dimensions) and  $C_1$  is a 2:1 spiral saddle. By “connected” we mean that the 2D unstable manifold  $W^u(C_0)$  and the 2D stable manifold  $W^s(C_1)$  intersect. The intersection is then a set of saddle connectors. If the spiraling at both  $C_0$  and  $C_1$  is sufficiently strong, the surface pair  $(W^u(C_0), W^s(C_1))$  roughly delimits a recirculation region. In its simplest form this region is a vortex ring, as is illustrated in Figure 1. The saddle connectors alone give already some idea of the geometry of the recirculation region. However, there is usually more topological information available for visualization than just the saddle connectors. Such features include chaotic regions, islands of stability, and invariant tori having rational or irrational rotation numbers (i.e. frequency ratios).

If the (3D) vector field is divergence-free any such transversal intersection of the 2D (un-)stable manifolds of two spiral saddles with sufficient spiraling automatically implies a heteroclinic tangle. This phenomenon which is also known as Shilnikov chaos [Sil65, SVL01] is well known in the dynamical systems literature and can be described as follows. In general, the two manifolds  $W^u(C_0)$  and  $W^s(C_1)$  do not coincide, but intersect transversally. In this case they intersect at an even number of saddle connectors, usually a pair  $\sigma$  and  $\sigma'$  of them. Between the windings of the saddle connectors, the manifolds form two “tubes” that are wrapped around the structure. The tubes have constant flux (i.e. independent of cross sections) because the 2D manifolds are stream surfaces, and the sum of the two fluxes is zero because of the divergence-free condition. This implies that toward the critical points, where velocities approach zero, the tubes must either have increasing cross section

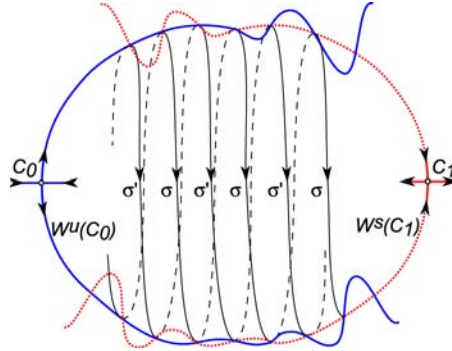


**Fig. 1.** Unstable manifold (blue) and stable manifold (red) of spiral saddles  $C_0$  and  $C_1$ , respectively. Their intersection is a pair of saddle connectors  $\sigma$  and  $\sigma'$ .

area or develop folds that extend into regions of higher velocities. These folds, known as lobes, are typical of vortex breakdown bubbles (see e.g. [SMH98]). It might seem strange to use the term vortex ring not only for structures such as smoke rings but also for the chaotic structure of a vortex breakdown bubble. However, this is consistent with the literature [KF02].

Much of dynamical systems theory deals with the special case of Hamiltonian systems, because of their area-conserving maps which are mainly responsible for chaotic behavior. Among the vector fields, the divergence-free ones play a similar role, and in fact they are related to Hamiltonian systems. In 2D, divergence free-vector fields (written as ODEs) and Hamiltonian systems are even the same, with the stream function  $\Psi$  (with  $\frac{\partial \Psi}{\partial x} = -\dot{y}$  and  $\frac{\partial \Psi}{\partial y} = \dot{x}$ ) playing the role of the Hamiltonian function. In 3D, a divergence-free vector field is volume preserving, but does not necessarily have area-conserving Poincaré maps. Nevertheless, the Poincaré map is at least flux-conserving, which is the reason for the above mentioned Shilnikov chaos to occur.

The use of topological methods for time-dependent flow is sometimes questioned. Haller [Hal01] says that structures such as chaotic tangles or KAM tori (i.e. invariant tori of a Hamiltonian system) do not exist in finite-time turbulent data sets. Nevertheless we believe that it is interesting to search for such structures, first of all in steady flow fields (where time can be viewed as infinite). It can be demonstrated that these topological features exist in practical flow data, meaning that the catalog of features to be studied in vector field topology must include invariant tori, chaotic regions, intersecting stable and unstable manifolds and multiple saddle connectors. Clearly, the definition of stable and unstable manifolds requires infinite-time flows, but this already holds for the separatrices in the commonly treated 2D case. Practical flow has often small enough time-dependence that their visualization as steady flow is a good enough approximation. The fact that vortex breakdown bubbles have been photographed in experiments [SMH98] confirms that this holds even if chaos is involved. Furthermore, the shapes observed in experiments have been

shown to be consistent with the manifolds of critical points in a steady vector field [SVL01].

### 3 Analytical vortex ring model

For testing our algorithms, we developed a simple analytic vortex ring model based on Hill's spherical vortex (see e.g. [Saf92]). An analytical vector field has the advantage that artifacts due to discretization and interpolation can be excluded. A second motivation was to demonstrate that a rich topology (Figure 7) is possible even if the vector field has only two critical points and can be expressed with only quadratic terms (Eq. 3).

An instance of Hill's spherical vortex can be described by the two velocity fields

$$\mathbf{u}^i(x, y, z) = \begin{pmatrix} xz \\ yz \\ z^2 + 1 - 2r^2 \end{pmatrix} \quad (1)$$

for points inside the unit sphere  $r = \sqrt{x^2 + y^2 + z^2} \leq 1$  and

$$\mathbf{u}^o(x, y, z) = \begin{pmatrix} xzr^{-5} \\ yzr^{-5} \\ z^2r^{-5} - \frac{1}{3}r^{-3} - \frac{2}{3} \end{pmatrix} \quad (2)$$

for points outside it ( $r \geq 1$ ).

The field is divergence-free, and it solves the Navier-Stokes equations (together with a matching pressure field). Furthermore, the field has zero vorticity outside the unit sphere. See Figure 2.

By adding a swirl  $(\omega y, -\omega x, 0)$ , a rotating vortex ring model is obtained. This simple model does not solve the Navier-Stokes equations but is capable of generating the topological phenomena that can be observed in vortex rings. Physically correct variants of Hill's vortex with swirl exist, but they are more expensive to compute since Bessel functions have to be evaluated [Saf92]. A different kind of generalization of Hill's spherical vortex are the Norbury vortex rings [Nor73] where the vorticity is confined to toroidal regions instead of the sphere.

In order to obtain the chaotic behavior of a real vortex ring, the symmetry must be broken. In our model we do this by tilting the x-axis, which is motivated by experimental studies of vortex rings (see [TH03]). By substituting  $z' = z + \epsilon x$  for  $z$  and  $w' = w + \epsilon u$  for  $w$  in Eq. 1, and by adding the swirl, we get the velocity fields

$$\mathbf{u}_{\epsilon\omega}^i(x, y, z) = \begin{pmatrix} \omega y \\ -\omega x \\ 0 \end{pmatrix} + \begin{pmatrix} xz' \\ yz' \\ zz' + 1 - 2r'^2 \end{pmatrix} \quad (3)$$

for points inside the distorted unit sphere  $r' = \sqrt{x^2 + y^2 + z'^2} \leq 1$  and

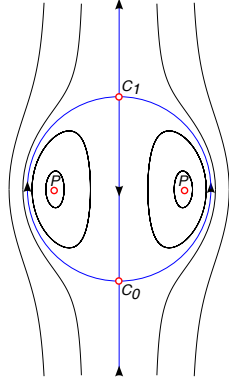


**Fig. 2.** Hill's spherical vortex (axial slice).  $C_0, C_1$ : critical points (spiral saddles),  $P$ : periodic orbit.



**Fig. 3.** Hill's spherical vortex with swirl ( $\omega = 2\pi$ ) and tilt ( $\epsilon = 0.313$ ). Slice of the stable manifold of the critical point at  $(0, 0, 1)$ .

$$\mathbf{u}_{\epsilon\omega}^o(x, y, z) = \begin{pmatrix} \omega y \\ -\omega x \\ 0 \end{pmatrix} + \begin{pmatrix} xz'r'^{-5} \\ yz'r'^{-5} \\ zz'r'^{-5} - \frac{1}{3}r'^{-3} - \frac{2}{3} \end{pmatrix} \quad (4)$$

for points outside of it.

This modified field is still divergence-free. It can be shown that the only critical points are two spiral saddles at  $(0, 0, -1)$  and  $(0, 0, 1)$ .

Figure 6 shows a  $x = 0$  slice of the unstable manifold of the critical point at  $(0, 0, 1)$ , computed by seeding 200000 streamlines near the critical point and allowing for a maximum of 200000 intersections with the plane. The coloring of intersection points represents time, expressed in number of intersections with the plane. A rainbow color map is used, starting with violet and ending with red for intersection number 1000 and above. The system of three ODEs was solved with the 4<sup>th</sup> order Runge-Kutta-Fehlberg routine from the Netlib library.

If an even simpler model is needed, it is also possible to use just the inner part  $\mathbf{u}_{\epsilon\omega}^i$  for the entire domain, see Figure 7.

## 4 Visualization techniques for vortex rings

The visualization technique we propose for vortex rings consists of three steps. First, the set of critical points is computed, and candidates for vortex rings are generated among pairs of spiral saddles of opposite type. Then, a plane passing through the two critical points is chosen, and a Poincaré section of  $W^u(C_0)$  and  $W^s(C_1)$  is taken. If an intersection of these is observed, the vortex ring is confirmed. Finally, the Poincaré section is used to extract islands of stability, i.e. to segment regions of chaotic and ordered flow.

#### 4.1 Detection of vortex rings

The set of critical points is computed with the standard cell-by-cell method. Only cells where all three vector components have a zero crossing have to be processed. For classifying the critical points, the eigenvalues of the Jacobian are needed. One positive real eigenvalue and a pair of complex eigenvalues with negative real parts indicate a 2:1 spiral saddle, while opposite signs indicate a 1:2 spiral saddle. Pairs  $(C_0, C_1)$  of these two kinds of spiral saddles are now taken as candidates for vortex rings. We choose pairs simply based on vicinity and leave it to the verification step described in Section 4.2 to eliminate wrong pairs. Alternatively one could extract vortex core lines and make use of the fact that critical points of spiral saddle type lie on core lines because they fulfill both the Sujudi-Haines and Levy criterion. Yet another approach would be to compute the set of saddle connectors which gives the correct pairs directly.

#### 4.2 Poincaré section

We choose a plane passing through  $C_0$  and  $C_1$ , using the remaining degree of freedom to fit the plane to the two real eigenvector directions of the two critical points. This way, the section is taken close to the center line of the vortex ring. Then a uniform grid is defined on the plane with an extent chosen based on the distance  $d = \|C_1 - C_0\|$ . We found a square with edge length  $2d$  to be sufficient in most cases. The two manifolds  $W^u(C_0)$  and  $W^s(C_1)$  are now computed based on a discrete set of seed points, and the intersections with the Poincaré section are stored as two (texture) images. Seed points for the manifold of, say,  $C_0$  are generated as follows. A first seed  $s_0$  is chosen at a small offset from  $C_0$  on the Poincaré plane where it intersects the plane spanned by the two complex eigenvectors. From  $s_0$ , a streamline is integrated in the time direction where the distance from  $C_0$  increases. Its next iterate (i.e. intersection with the Poincaré plane) is denoted by  $s_1$ . Further seed points are now generated on the straight line segment between  $s_0$  and  $s_1$  by logarithmically interpolating the distance of the seed points to  $C_0$ . Logarithmic interpolation is appropriate because close to  $C_0$  streamlines are logarithmic spirals, and the error introduced by interpolating along a straight line falls off with the streamlines converging to the 2D manifold.

Integrating streamlines for all seed points and for a given maximum number of intersections with the Poincaré plane results in an image showing the intersection curve of the 2D manifold. By overlaying the images of  $C_0$  and  $C_1$  it can be decided if the manifolds intersect. An example pair is shown in Figure 10. In that case the image shows the lobes (folds) extending toward the second critical point. It also shows the chaotic region formed by the inward extending lobes, and it typically shows a hierarchy of islands of stability. The islands of stability are toroidal regions around a periodic orbit of minimal period. The inner part of stability islands is typically filled with nested invariant tori with no flux across them (stream surfaces, known as KAM tori in the

case of Hamiltonian systems). Further out, chains of secondary islands can often be seen. These can be separated from the primary island by first regions of chaos. When the chaotic region is reached, so-called cantori [MMP84] can appear. These are porous tori of measure zero, which in some cases (if the rotation number is a “noble” irrational number) have very little flux across them, and act therefore as partial barriers.

### 4.3 Islands of stability

From the previous step the Poincaré sections of  $W^u(C_0)$  and  $W^s(C_1)$  are now given as scalar fields on a regular 2D grid (or image) where the data values (or color indices) store the integration time or zero for cells that were not intersected. The goal is now to segment in the overlay of the two images the islands of stability. First, to clean the boundaries, a morphological closure operation is performed. This is followed by a component labeling step. Any component which does not extend to the image boundary is now checked for being an island of stability. A problem here is to distinguish islands of stability from holes that are formed by inward folding lobes. It can be observed that the latter are reached after much shorter integration time, hence when the average data value on their boundary is computed, this value is small compared to that of stability islands (see Figures 6, 7, 9, 10).

The obtained candidates for islands of stability are now processed in order of decreasing size. First, a streamline is seeded at the center of the island’s bounding rectangle and whenever the Poincaré plane is intersected, the labeled component of the intersection point is marked as being part of the same island. If the streamline intersects the Poincaré section at a point outside of a component with a valid label, the test has failed.

Given now an island of stability, we want to visualize its internal structure which is a periodic orbit surrounded by nested invariant tori, with possible island chains interspersed in the outer part. For the Hill’s vortex example, the primary and secondary islands are shown in Figure 4.

We will visualize as two characteristic features the periodic orbit in the center and the outermost torus. The streamline seeded at the center of the island’s bounding rectangle is integrated for a few “rounds” (detectable by increasing/decreasing  $x$  and  $y$  coordinates in the Poincaré plane). This should produce a set of points lying densely on a closed curve, otherwise it has to be retried from a slightly offset seed point. If a closed curve is obtained, the center of its bounding rectangle can be used for the next iteration of the process which is repeated until a fixed point is found.

This algorithm exploits the special structure of nested tori and is significantly faster than the general approach of looking for fixed points of the Poincaré map, especially since in the case of secondary islands no fixed points are found and successive powers of the Poincaré map must be computed and searched for fixed points, too.

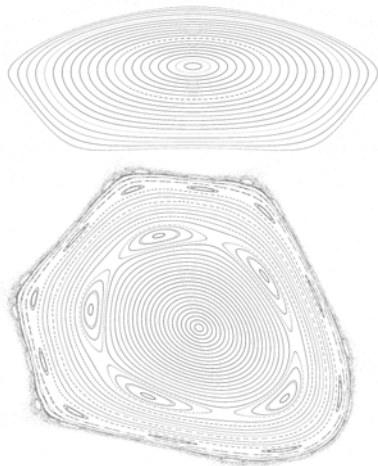


**Fig. 4.** Internal structure of primary and secondary island of Figure 3.



**Fig. 5.** Primary (yellow) and secondary (red) islands rendered as stream surfaces.

For finding the boundary of the island of stability, an iterative search is started with a seed curve consisting of the outermost black (zero) pixels. At pixels which are mapped to a pixel outside the boundary, the seed curve is corrected inward by a pixel. This is repeated until all pixels of the seed curve are mapped to pixels inside the island. Finally, on these pixels the map is iterated a few times in order to reach a fixed curve. The obtained curve can be used as a seed curve for a simplified stream surface algorithm which requires only integration until the same component of the Poincaré plane is intersected again. Figure 5 shows a pair of stream surfaces obtained this way.

With a similar technique, the manifolds  $W^u(C_0)$  and  $W^s(C_1)$  can be obtained as stream surfaces with seed curves extracted from the Poincaré section. The stream surface can of course be computed directly, but this requires a robust algorithm to cope with the highly curved lobes.

## 5 Results

We applied the techniques described in Section 4 to two CFD simulation results. In both cases, the data are given at the nodes of unstructured hexahedral grids. In principle, the computed velocity fields are divergence-free, however this is only true for the integrals over the control volumes, but not for the trilinearly interpolated data. Since we observed that any residual divergence left in the data causes the chaotic region to shrink, we did a divergence cleaning of the data prior to the visualization. The standard method for divergence cleaning is the Hodge projection method [BB80, Tot00] which is based on

the decomposition of  $\mathbf{u}$  into a divergence-free part and an irrotational part,  $\mathbf{u} = \mathbf{u}_0 + \nabla s$ . It follows  $\nabla \cdot \mathbf{u} = \nabla \cdot \nabla s$  which is a Poisson equation for  $s$ .

### 5.1 Vortex ring in Francis draft tube

In the time-dependent simulation of the draft tube of a Francis turbine, we found a vortex ring extending spanwise and with a temporally quite stable behavior. An overview of the flow with the vortex ring and the rectangle used for the Poincaré section can be seen in Figure 8. The stable and unstable 2D manifolds of the two critical points show the structure of the vortex ring with two primary islands of stability, see Figure 10. The abrupt change of colors near the islands of stability corresponds to jumps in integration time and therefore indicates cantori. These are toroidal surfaces which act as partial barriers for the mixing of the fluid.

In an earlier paper [SP07], we visualized the same flow structure with a volumetric technique but without divergence cleaning. As a result, most of the chaotic folding was lost because the flow was quickly attracted to a toroidal surface.

### 5.2 Vortex ring in simulation of a river power plant

Our second example is the flow in a river power plant developing two large vertical vortices at the surface, see Figure 9. We selected the left one of them, and chose a Poincaré section in the vertical plane through the two critical points. The result is shown in Figure 11.

In this example, the vortex ring extends to the (free slip) water surface where one of the two spiral saddles is located. The unstable manifold of the latter coincides with the stable manifold of a periodic orbit of saddle type which is also located at the water surface. In order to be able to integrate streamlines at the water surface, the normal velocity component had to be set to exactly zero, i.e. residual normal velocities from the simulation had to be removed.

The seemingly ring-shaped lobes are an artifact of the slice plane which does not follow well the curved center line of the structure. The effective shape of the lobes is similar to the one in Figure 4.

## 6 Conclusion

We presented an algorithm for finding vortex rings in velocity fields and visualizing them by means of a Poincaré section. Based on the latter, we described how islands of stability can be identified and seed curves for invariant tori are obtained, in particular for the outermost of the nested tori. A fast method was presented for computing the central periodic orbit of an island of stability.

By applying these techniques to CFD data, we were able to find vortex rings and visualize them. Finally, we developed an analytical model of a perturbed vortex ring.

Part of the underlying theory requires divergence-free vector fields and thus incompressible flow. However, some of the proposed visualization techniques are also applicable to compressible flow. As an interesting future work we see the application of the proposed techniques, possibly modified, to examples of compressible flow such as smoke rings.

Although most of the vortex rings we found in CFD results contain just two critical points, some others have four or more of them. Additional critical points appear during events such as merging or splitting of vortex rings. Often there are small additional vortex rings which exist only for a short time and can thus be considered as noise. It would be an interesting topic to study how the various topology simplification techniques could improve our visualization technique.

## Acknowledgment

We thank the anonymous reviewers for their valuable suggestions and France Suerich-Gulick for the river power plant data. This work was supported by the Swiss Commission for Technology and Innovation (CTI) under grant 7338.2 ESPP-ES.

## References

- [AS92] ABRAHAM R. H., SHAW C. D.: *Dynamics, the Geometry of Behavior*. 2nd ed. Addison-Wesley, 1992.
- [BB80] BRACKBILL J., BARNES D.: The effect of nonzero  $\nabla \cdot \mathbf{B}$  on the numerical solution of the magnetohydrodynamic equations. *J. Comput. Phys.* 35 (1980), 426430.
- [GH83] GUCKENHEIMER J., HOLMES P.: *Nonlinear Oscillations, Dynamical Systems and Bifurcations of Vector Fields*. Applied Mathematical Sciences, Vol. 42. Springer, New York, Berlin, Heidelberg, Tokyo, 1983.
- [GLL91] GLOBUS A., LEVIT C., LASINSKI T.: A tool for visualizing the topology of three-dimensional vector fields. In *Proc. IEEE Visualization '91* (1991), pp. 33–40.
- [GTS\*04] GARTH C., TRICOCHÉ X., SALZBRUNN T., BOBACH T., SCHEUERMANN G.: Surface techniques for vortex visualization. In *VisSym* (2004), pp. 155–164, 346.
- [Hal01] HALLER G.: Lagrangian structures and the rate of strain in a partition of two-dimensional turbulence. *Phys. Fluids* 13 (2001), 3365–3385.
- [HH89] HELMAN J., HESSELINK L.: Representation and display of vector field topology in fluid flow data set. *IEEE Computer* (August 1989), 27–36.
- [KF02] KRASNY R., FRITSCHÉ M.: The onset of chaos in vortex sheet flow. *J. Fluid Mech.* 454 (2002), 47–69.

- [LDG98] LÖFFELMANN H., DOLEISCH H., GRÖLLER E.: Visualizing dynamical systems near critical points. In *14th Spring Conference on Computer Graphics* (April 1998), Kalos L. S., (Ed.), pp. 175–184.
- [LG98] LÖFFELMANN H., GRÖLLER E.: Enhancing the visualization of characteristic structures in dynamical systems. In *Visualization in Scientific Computing '98* (1998), Bartz D., (Ed.), Springer, pp. 59–68.
- [LKG97] LÖFFELMANN H., KUCERA T., GRÖLLER E.: Visualizing poincaré maps together with the underlying flow. In *Mathematical Visualization. Proceedings of the International Workshop on Visualization and Mathematics '97* (1997), Hege H.-C., Polthier K., (Eds.), Springer, pp. 315–328.
- [MMP84] MACKAY R. S., MEISS J. D., PERCIVAL I. C.: Transport in hamiltonian systems. *Physica D 13D* (1984), 55–81.
- [Nor73] NORBURY J.: A family of steady vortex rings. *J. Fluid Mech.* 57, Pt. 3 (1973), 417–431.
- [Saf92] SAFFMAN P. G.: *Vortex Dynamics*. Cambridge Univ. Press, Cambridge, UK, 1992.
- [Sil65] SIL'NIKOV L. P.: A case of the existence of a denumerable set of periodic motions. *Sov. Math. Dokl.* 6 (1965), 163–166.
- [SMH98] SPOHN A., MORY M., HOPFINGER E.: Experiments on vortex breakdown in a confined flow generated by a rotating disc. *Journal of Fluid Mechanics* 370 (1998), 73–99.
- [SP07] SADLO F., PEIKERT R.: Topology-guided visualization of constrained vector fields. In *Proceedings of the 2005 Workshop on Topology-Based Methods in Visualization, Budmerice, Slovakia* (2007), p. (to appear).
- [SVL01] SOTIROPOULOS F., VENTIKOS Y., LACKEY T. C.: Chaotic advection in three-dimensional stationary vortex-breakdown bubbles: Sil'nikov's chaos and the devil's staircase. *J. Fluid Mech.* 444 (2001), 257–297.
- [SZH97] STALLING D., ZÖCKLER M., HEGE H.-C.: Fast display of illuminated field lines. *IEEE Transactions on Visualization and Computer Graphics* 3, 2 (1997), 118–128.
- [TGK\*04] TRICOCHÉ X., GARTH C., KINDLMANN G., DEINES E., SCHEUERMANN G., RUETTEN M., HANSEN C.: Visualization of intricate flow structures for vortex breakdown analysis. In *Proc. IEEE Visualization 2004* (October 2004), IEEE Computer Society, pp. 187–194.
- [TH03] THOMPSON M. C., HOURIGAN K.: The sensitivity of steady vortex breakdown bubbles in confined cylinder flows to rotating lid misalignment. *Journal of Fluid Mechanics* 496 (Dec. 2003), 129–138.
- [Tot00] TOTTH G.: The  $\text{div } \mathbf{b}=0$  constraint in shock-capturing magnetohydrodynamics codes. *Journal of Computational Physics* 161 (2000), 605–652.
- [TWH03] THEISEL H., WEINKAUF T., HEGE H.-C., SEIDEL H.-P.: Saddle connectors - an approach to visualizing the topological skeleton of complex 3d vector fields. In *Proc. IEEE Visualization 2003* (Oct. 2003), pp. 225–232.
- [WHN\*03] WEINKAUF T., HEGE H.-C., NOACK B., SCHLEGEL M., DILLMANN A.: Coherent structures in a transitional flow around a backward-facing step. *Physics of Fluids* 15, 9 (September 2003), S3.
- [WS01] WISCHGOLL T., SCHEUERMANN G.: Detection and visualization of closed streamlines in planar flows. *IEEE Transactions on Visualization and Computer Graphics* 7, 2 (2001), 165–172.
- [YKP05] YE X., KAO D., PANG A.: Strategy for scalable seeding of 3d streamlines. In *Proc. IEEE Visualization '05* (2005), pp. 471–478.

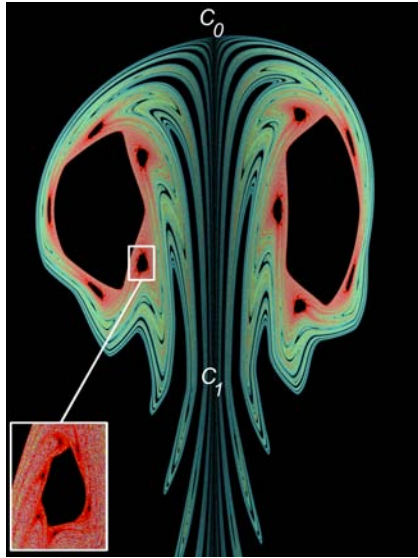


**Fig. 6.** Hill's spherical vortex with swirl ( $\omega = 2\pi$ ) and tilt ( $\epsilon = 0.313$ ). Slice of the stable manifold of the critical point at  $(0, 0, 1)$ .

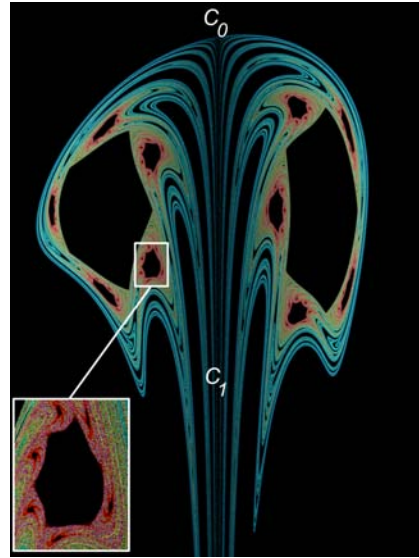


**Fig. 7.** Inner part  $\mathbf{u}_{\epsilon\omega}^i$  of Hill's spherical vortex with swirl ( $\omega = 2\pi$ ) and tilt ( $\epsilon = 0.442$ ).

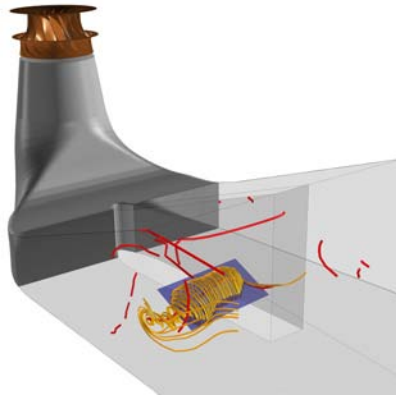


**Fig. 8.** Overview of the flow in the draft tube. Poincaré section used for Figure 10 shown as blue rectangle, vortex core lines shown in red.

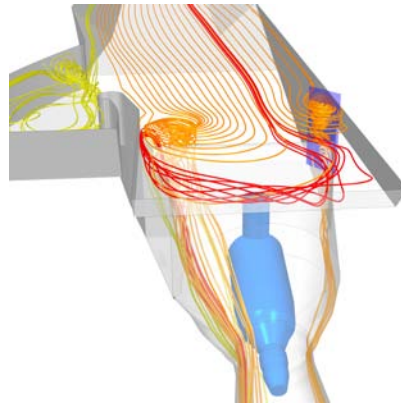


**Fig. 9.** Overview of the flow in the river power plant. Poincaré section used for Figure 11 shown as blue rectangle.

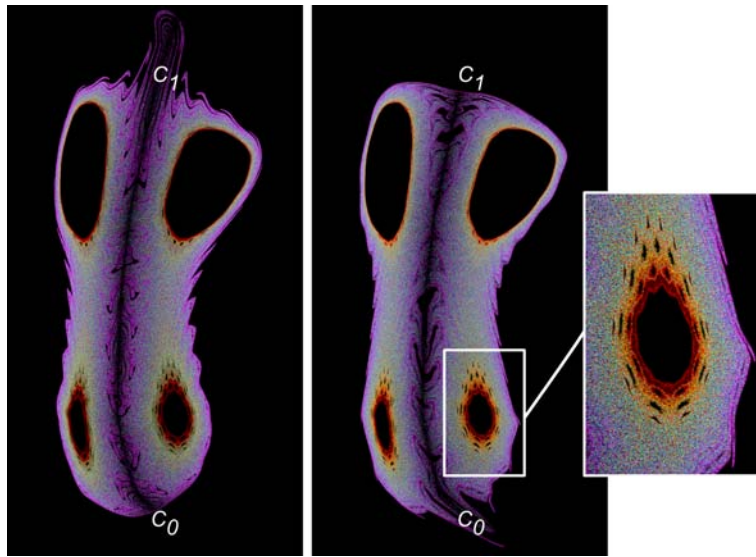


**Fig. 10.** Stable (left) and unstable (right) manifolds of vortex ring in draft tube dataset.

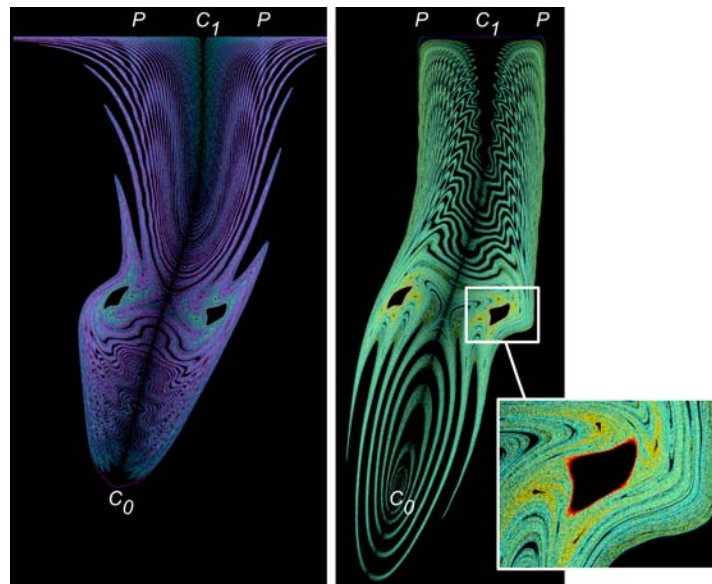


**Fig. 11.** Left: Stable manifold of spiral saddle  $C_0$  in river power plant dataset. Right: unstable manifold of periodic orbit  $P$ , approximated by seeding just below spiral saddle  $C_1$ , close-up on primary island of stability.